2014-09

Microwave hydrothermal synthesis, characterisation, and catalytic performance of Zn1xMnxO in cellulose conversion

Chemical Papers,Bratislava : Slovak Academy of Sciences - Institute of Chemistry,v. 68, n. 9, p. 1213-1218, Sept. 2014

http://www.producao.usp.br/handle/BDPI/51349

VERSITA

Chemical Papers 68 (9) 1213–1218 (2014)
DOI: 10.2478/s11696-013-0468-8

ORIGINAL PAPER

Microwave hydrothermal synthesis, characterisation, and catalytic performance of $Zn_{1-x}Mn_xO$ in cellulose conversion

[a]Maria I. B. Bernardi, [a]Vinícius D. Araújo, [b]Caue Ribeiro, [b,c]Waldir Avansi, [c]Elson Longo, [d]Nilson J. A. de Albuquerque, [d]Simoni M. P. Meneghetti, [d]Rusiene M. Almeida, [e]Humberto V. Fajardo*

[a]*Institute of Physics – USP, 13560-970, São Carlos – SP, Brazil*

[b]*National Nanotechnology Laboratory for Agribusiness – EMBRAPA, 13560-970, São Carlos – SP, Brazil*

[c]*Institute of Chemistry – UNESP, 14800-900, Araraquara – SP, Brazil*

[d]*Institute of Chemistry and Biotechnology – UFAL, 57072-970, Maceió – AL, Brazil*

[e]*Department of Chemistry – UFOP, 35400-000, Ouro Preto – MG, Brazil*

Received 26 February 2013; Revised 3 June 2013; Accepted 28 June 2013

Wurtzite-type $Zn_{1-x}Mn_xO$ (x = 0, 0.03, 0.05, 0.07) nanostructures were successfully synthesised using a simple microwave-assisted hydrothermal route and their catalytic properties were investigated in the cellulose conversion. The morphology of the nanocatalysts is dopant-dependent. Pure ZnO presented multi-plate morphology with a flower-like shape of nanometric sizes, while the $Zn_{0.97}Mn_{0.03}O$ sample is formed by nanoplates with the presence of spherical nanoparticles; the $Zn_{0.95}Mn_{0.05}O$ and $Zn_{0.93}Mn_{0.07}O$ samples are mainly formed by nanorods with the presence of a small quantity of spherical nanoparticles. The catalyst without Mn did not show any catalytic activity in the cellulose conversion. The Mn doping promoted an increase in the density of weak acid sites which, according to the catalytic results, favoured promotion of the reaction.

Keywords: zinc oxide, catalysts, hydrothermal synthesis, cellulose

Introduction

The use of different synthesis routes has afforded materials with novel properties and applications. Of these routes, the hydrothermal process is prominent in terms of its control of the synthesis parameters, thus facilitating the aquisition of samples with different morphologies and structures. The microwave-assisted solvo-thermal method combines the advantages of both hydrothermal and microwave-irradiation techniques such as a brief reaction time and the production of small particles with a narrow size distribution and high purity which might be attributed to the rapid and homogeneous nucleation of the mixture. The effect of heating is created by the interaction of the dipole moment of the molecules with the high-frequency electromagnetic radiation (2.45 GHz). The microwave-heating method has recently attracted the attention due to its very short reaction time, its production of small particles with narrow particle size distribution and its low energy consumption compared with conventional methods (Avansi et al., 2011; Oliveira et al., 2011; Zhang et al., 2011; Zou et al., 2012; Robles-Nuñez et al., 2012). Within this context, this work aims, via the microwave-assisted method, to perform the synthesis of pure zinc oxide and zinc oxide doped with manganese. These oxides have attracted attention due to their chemical and physical properties

*Corresponding author, e-mail: hfajardo@iceb.ufop.br

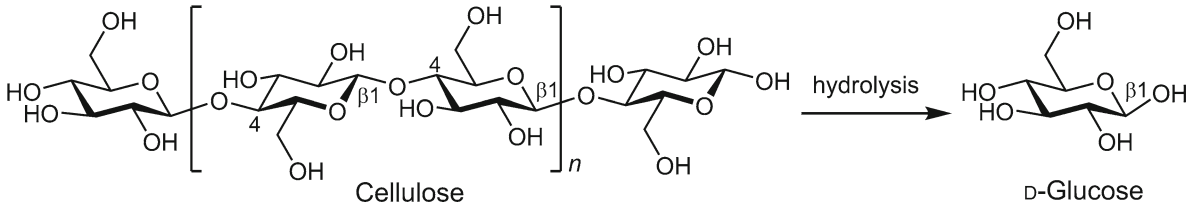

Fig. 1. Equation illustrating cellulose hydrolysis reaction.

for a wide range of applications (Milao et al., 2012). The morphological and structural characterisations of the samples as-obtained, as well as a preliminary study of their catalytic properties in the hydrolysis of cellulose reaction (Fig. 1), are reported here. Cellulose is a natural product with remarkable potential for use as an environmentally friendly alternative to fossil resources for the sustainable production of useful fuels and chemicals. Traditionally, catalytic systems based on enzymes, dilute acids, and supercritical water are employed in the above process; however, these have significant disadvantages such as high costs, corrosion hazard, low reaction rates, and difficulties in the separation of products and catalysts. To overcome these problems, the use of heterogeneous catalysts in this process has attracted a great deal of interest due to the large potential, both in terms of their activity and selectivity and the possibility of developing a clean technology (Huber et al., 2006; Luo et al., 2007; Onda et al., 2008; Komanoya et al., 2011). Noble metal-based catalysts have been extensively studied in the cellulose conversion reactions and frequently exhibit high activity. However, they are expensive, hence their use could represent an economic obstacle to the whole process. To the best of our knowledge, this is the first report of the use of $Zn_{1-x}Mn_xO$ nanostructures, synthesised via the microwave-assisted hydrothermal method, as catalysts in the hydrolysis of cellulose.

Experimental

$Zn_{1-x}Mn_xO$ (x = 0, 0.03, 0.05, 0.07) nanostructures were synthesised using $Zn(NO_3)_2 \cdot 6H_2O$ (Aldrich) and $Mn(NO_3)_2 \cdot 6H_2O$ (Aldrich) as precursors. In a typical procedure, the precursor (0.05 mol) was dissolved in distilled water (50 mL) followed by the rapid addition of NaOH solution (3 mol L^{-1}, 50 mL) under vigorous stirring and subsequent loading into an autoclave, which was sealed and placed in the microwave-hydrothermal system using 2.45 GHz microwave radiation with a maximum power of 800 W. The solutions thus prepared were treated at 120 °C for 32 min at a heating rate of 30 °C min^{-1} and then air-cooled at ambient temperature. The powder precipitate was separated by centrifugation, washed with distilled water and dried at 60 °C for 24 h.

The samples were structurally characterised in an X-Ray diffractometer (Rigaku, Rotaflex RU200B) with Cu Kα radiation (50 kV, 100 mA, $\lambda = 1.5406$ Å), using a $\theta/2\theta$ configuration and a graphite monochromator. The scanning range was 10–90° (2θ), with a step size of 0.02° and a step time of 5.0 s. A Rietveld analysis was performed using the Rietveld refinement program GSAS (Larson & Von Dreele, 1994). A pseudo-Voigt profile function was used. The specific surface area (BET method) was estimated from the N_2 adsorption/desorption isotherms, using a Micromeritics ASAP 2020 particle size analyser. The sizes and morphologies of the samples were determined by electron microscopy using a field emission scanning electron microscope JEOL JSM 6701F. The NH_3 temperature-programmed desorption (NH_3-TPD) curves were obtained in a Quantachrome Instruments Chembet 3000 analyser and thermal conductivity detection with set data acquisition.

In the solubilisation, hydrolysis and cellulose degradation processes, microcrystalline cellulose (PH 101 AVICELTM, Fluka) was used with a particle diameter of 50 μm. The reactions were performed in a 200 mL stainless steel reactor coupled to pressure and temperature probes at 190 °C for 4 h with 0.48 g of cellulose, 60 mL of deionised water and 2.69×10^{-5} mol of catalyst. Following the reaction, the mixture was filtered through filter paper and the unconverted cellulose was dried at 90 °C for 24 h, with subsequent gravimetric evaluation of cellulose conversion using Eq. (1),

$$C = \left(\frac{m_0 - m_f}{m_0}\right) \times 100 \qquad (1)$$

where C is the cellulose conversion (cellulose consumption percentage); m_0 is the initial cellulose mass (g) and m_f is the unconverted cellulose mass (g).

Results and discussion

Fig. 2 shows the X-ray diffraction patterns of the $Zn_{1-x}Mn_xO$ samples. A comparison of the d-values observed in the ZnO samples with the standard (ICSD file no. 36-1451) clearly revealed the formation of stable monophasic zincite with a hexagonal (wurtzite-type) crystal structure of ZnO. For the $Zn_{1-x}Mn_xO$ samples (x = 0.03, 0.05, 0.07), discrete peaks of a $ZnMn_2O_4$ second phase appear (ICSD file no. 16-6522), as shown in Table 1. The cell parameter values for the $Zn_{1-x}M_xO$ samples obtained are between the

Table 1. Characterisation data: Lattice parameter, R_{wp}, R_{exp}, R_{Bragg}, S^2, cell volume (V) and density (ρ), surface area (A), crystallite size (D), and catalytic activity (C) for the $Zn_{1-x}Mn_xO$ samples

Parameter	ZnO	$Zn_{0.97}Mn_{0.03}O$	$Zn_{0.95}Mn_{0.05}O$	$Zn_{0.93}Mn_{0.07}O$
R_{wp}/%	8.19	10.57	12.31	13.33
R_{exp}/%	13.32	11.43	5.82	4.93
S^2	1.23	1.85	4.23	5.41
R_{Bragg}/%	2.60	4.90	5.54	6.49
$a = b$/Å	3.2520 ± 0.0001	3.2522 ± 0.0001	3.2525 ± 0.0001	3.2523 ± 0.0001
c/Å	5.2103 ± 0.0001	5.2106 ± 0.0001	5.2134 ± 0.0001	5.2131 ± 0.0001
Occ O	0.974 ± 0.006	0.976 ± 0.006	0.970 ± 0.008	0.98 ± 0.01
$\alpha = \beta$	90	90	90	90
γ	120	120	120	120
V/Å^3	47.719	47.728	47.764	47.754
Z	1	1	1	1
Space group	$P6_3/mc$	$P6_3/mc$	$P6_3/mc$	$P6_3/mc$
ρ/(g cm^{-1})	5.634	5.623	5.602	5.593
2th phase/%		2.13	4.23	5.49
A/(m^2 g^{-1})	12.2	15.2	16.4	18.5
D/nm	86	69	64	39
C/%	12	20	20	20

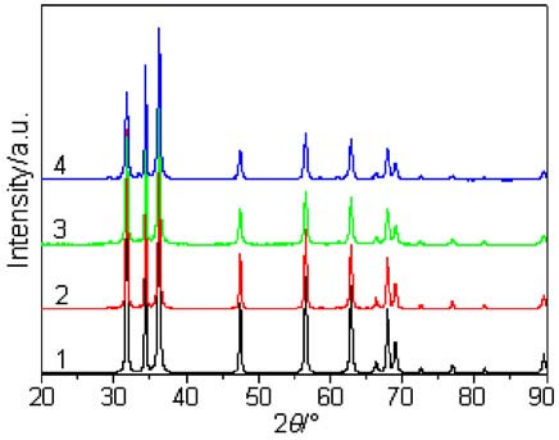

Fig. 2. XRD patterns of $Zn_{1-x}Mn_xO$ samples: ZnO (curve 1), $Zn_{0.97}Mn_{0.03}O$ (curve 2), $Zn_{0.95}Mn_{0.05}O$ (curve 3), $Zn_{0.93}Mn_{0.07}O$ (curve 4).

value $a = b = 3.2498$ Å, $c = 5.2066$ Å and $V = 47.62$ Å^3 corresponding to wurtzite structure ZnO. The addition of transition metals induces small changes in the unit cell dimensions. The changes in the lattice parameters are in accordance with the metal–oxygen distances due to the effective ionic radii of cations, as shown in Table 1 (Dondi et al., 2007).

Fig. 3 presents the FE-SEM images of the samples, rendering it possible to observe that the ZnO samples (Figs. 3a and 3b) are of multi-plate morphology with a flower-like shape of nanometric sizes. For the doped samples, a significant change in the function of the Mn content could be observed. For the $Zn_{0.97}Mn_{0.03}O$ sample (Figs. 3c and 3d), poorly formed nanoplates with the presence of spherical nanoparticles could be observed. On the other hand, the $Zn_{0.95}Mn_{0.05}O$ and $Zn_{0.93}Mn_{0.07}O$ samples (Figs. 3e–3h) present a morphology formed mainly by nanorods but still with the presence of a small quantity of spherical nanoparticles. Some authors have reported the change in morphology of synthesised samples related to dopant content, where the presence of the dopant modifies the surface energy (Stroppa et al., 2009). This research group recently reported the synthesis of ZnO and doped M : ZnO (M = V, Fe, and Co) nanostructures by similar microwave hydrothermal synthesis, showing that, for ZnO and doped M : ZnO (V and Co) samples, a similar flower-like morphology was obtained; however, the Fe : ZnO samples presented a poorly formed morphology (Milao et al., 2012).

An analysis of the NH_3-temperature-programmed desorption was performed to qualitatively determine the strength of the acid sites present in the samples (Fig. 4). The curves for ammonia desorption are generally classified into two regions: low temperature (LT, with temperature < 400 ℃) and high temperature (HT, with temperature > 400 ℃). The desorption in the HT region is associated with strong acid sites (Lewis and Brønsted) and the desorption in the LT region with weak acid sites (Kemdeo et al., 2010). The TPD patterns show major desorption peaks differing by samples in their positions and profiles, suggesting changes not only in the total acidity but also in the distribution of the acid strength in the samples. The TPD peaks for the $Zn_{0.95}Mn_{0.05}O$ and $Zn_{0.93}Mn_{0.07}O$ samples appear in the region of LT and also in HT, indicating the presence of both weak and strong acid sites on these catalysts (Azzouz et al., 2006).

One of the commonest ways to modify the characteristics of a material is by introducing dopants. When introduced into a powder, they may lead to surface modifications such as acid/base properties (Fajardo et al., 2008). The doped samples were observed to present smaller particle sizes than those that were not

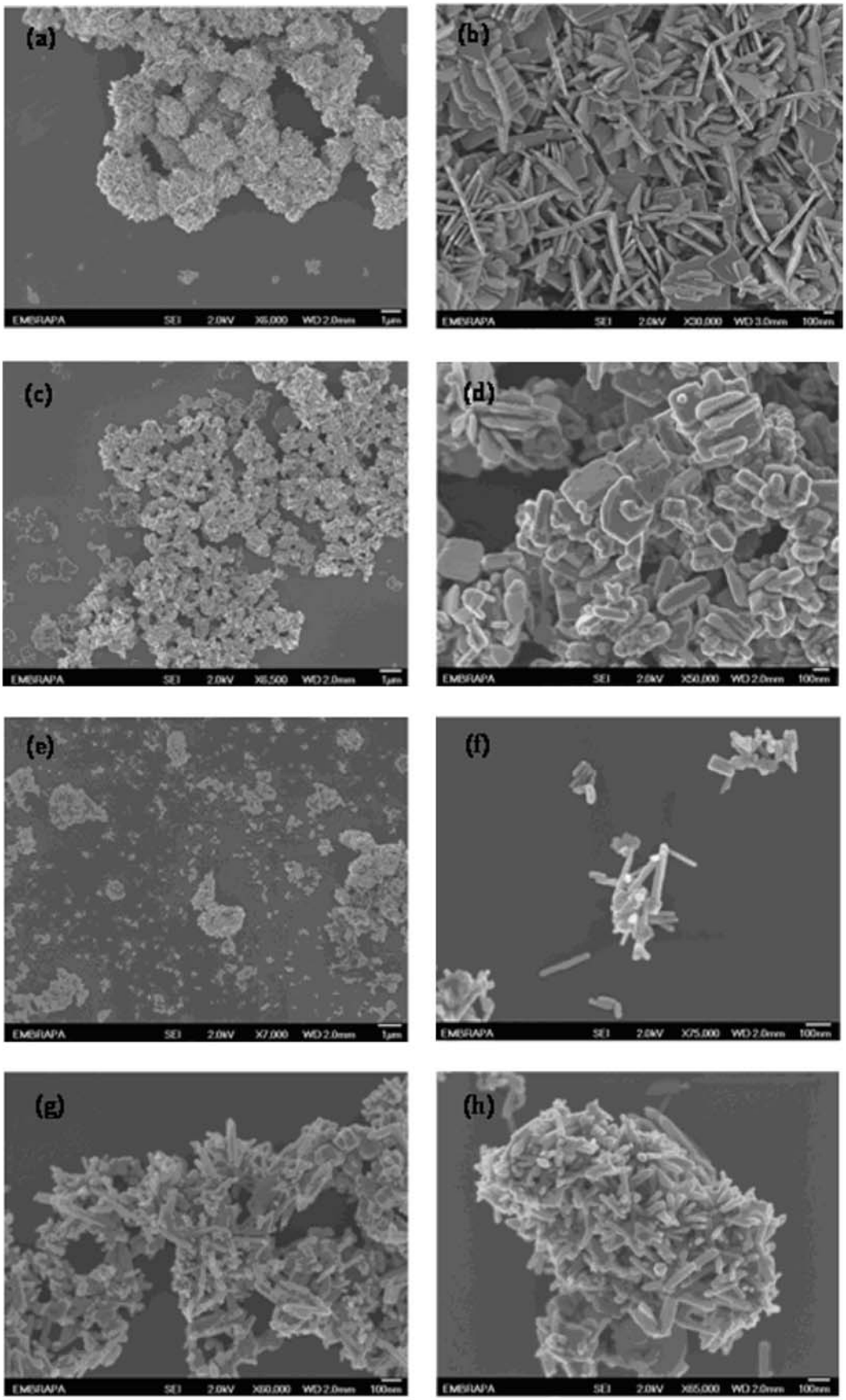

Fig. 3. FE-SEM images of samples: a) and b) ZnO; c) and d) $Zn_{0.97}Mn_{0.03}O$; e) and f) $Zn_{0.95}Mn_{0.05}O$; g) and h) $ZnO_{0.93}Mn_{0.07}O$.

Table 2. Percentage of soluble products identified from cellulose conversion promoted by $Zn_{1-x}Mn_xO$ samples

Products	ZnO	$Zn_{0.97}Mn_{0.03}O$	$Zn_{0.95}Mn_{0.05}O$	$Zn_{0.93}Mn_{0.07}O$
Glucose	2.8	4.2	4.8	4.7
Fructose	1.8	1.7	1.9	1.7
HMF	1.6	1.2	1.0	0.8
Lactic acid	4.4	4.4	5.1	5.0
Formic acid	–	–	1.1	1.3

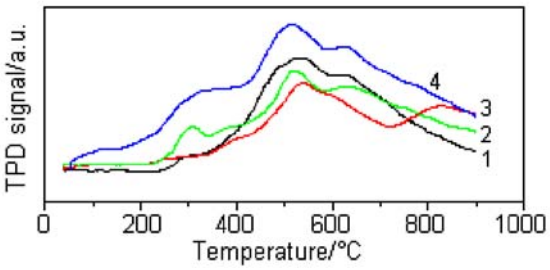

Fig. 4. NH_3-TPD profiles for $Zn_{1-x}Mn_xO$ samples: ZnO (curve 1), $Zn_{0.95}Mn_{0.05}O$ (curve 2), $Zn_{0.97}Mn_{0.03}O$ (curve 3), $Zn_{0.93}Mn_{0.07}O$ (curve 4).

doped. The decrease in the crystallite size due to the introduction of dopants led to an increase in the specific surface area (Table 1). However, the difference in such values cannot explain the difference in activity between the samples. From the results, the catalyst acidity appears to be effective for the reaction, but the activity does not accord very closely with the apparent acid strength of the catalysts. The Mn doping promoted an increase in the density of acid sites, especially in weak acid sites for the $Zn_{0.95}Mn_{0.05}O$ and $Zn_{0.93}Mn_{0.07}O$ samples in the temperature region between 240–340 °C (Fig. 4). The cellulose conversion is observed in all the Mn-doped catalysts; however, the NH_3-TPD curves show that the increase in the density of weak acid sites is not directly related to the increase in the cellulose conversion, indicating that the presence of weak acid sites of a moderate density is preferable or sufficient to promote the reaction. The catalyst without Mn did not exhibit any catalytic activity in the cellulose conversion; the conversion was the same as that without catalyst (Table 1). This is due to water being in the subcritical state, and acting as a catalyst in the hydrolysis process (Komanoya et al., 2011). The detection and quantification of the major reaction products formed (see Table 2) were made using the HPLC technique, as described by dos Santos et al. (2013). The catalytic species showed selectivity towards the formation of glucose, fructose, 5-(hydroxymethyl)furan-2-carbaldehyde (HMF), organic acids (lactic and formic acids) and traces of the cellobiose, 1,6-anhydroglucose, glyceraldehydes, and sorbitol. Note that glucose can also be converted to fructose by isomerisation and HMF can be obtained by the dehydration of hexoses (Girisuta et al., 2007; Corma et al., 2007), while the resulting HMF can be rehydrated to organic acids (Bicker et al., 2005). The doped catalysts promoted an increase in the glucose selectivity, which can be associated with the formation of weak acid sites, as shown by the NH_3-TPD measurements. The degradation reactions, responsible for the HMF and organic acids formation, can be associated with the synergy of weak and strong acid sites present on the catalyst surfaces.

Conclusions

$Zn_{1-x}Mn_xO$ nanostructures in a hexagonal (wurtzite-type) crystal structure phase were successfully synthesised using a simple microwave-assisted hydrothermal route. Additional peaks related to the $ZnMn_2O_4$ crystalline phase could be observed for the doped samples. The morphology of the nanocatalysts is dopant-dependent, revealing the formation of a multi-plate morphology with a flower-like shape for pure ZnO and the formation of nanoplates for the $Zn_{0.97}Mn_{0.03}O$ sample; nanorods were obtained for the $Zn_{0.95}Mn_{0.05}O$ and $Zn_{0.93}Mn_{0.07}O$ samples. The catalytic activity was not related to the catalyst morphology (shape and surface area); however the Mn doping promoted an increase in the density of weak acid sites which, according to the catalytic tests, favoured promotion of the reaction. These preliminary results show that $Zn_{1-x}Mn_xO$-prepared samples can convert cellulose and may be considered as a potential catalyst for application in the cellulose hydrolysis reaction.

Acknowledgements. The authors gratefully acknowledge FAPESP, CAPES, FAPEMIG and CNPq. The authors would also like to thank Prof. Jason G. Taylor for reviewing the English usage.

References

Avansi, W., Jr., Ribeiro, C., Leite, E. R., & Mastelaro, V. R. (2011). An efficient synthesis route of $Na_2V_6O_{16} \cdot nH_2O$ nanowires in hydrothermal conditions. *Materials Chemistry and Physics*, *127*, 56–61. DOI: 10.1016/j.matchemphys.2011.01.017.

Azzouz, A., Nistor, D., Miron, D., Ursu, A. V., Sajin, T., Monette, F., Niquette, P., & Hausler, R. (2006). Assessment of acid–base strength distribution of ion-exchanged montmorillonites through NH_3 and CO_2-TPD measurements. *Thermochimica Acta*, *449*, 27–34. DOI: 10.1016/j.tca.2006.07.019.

Bicker, M., Endres, S., Ott, L., & Vogel, H. (2005). Catalytical conversion of carbohydrates in subcritical water: A new chemical process for lactic acid production. *Journal of Molecular Catalysis A: Chemical*, *239*, 151–157. DOI: 10.1016/j.molcata.2005.06.017.

Corma, A., Iborra, S., & Velty, A. (2007). Chemical routes for the transformation of biomass into chemicals. *Chemical Reviews*, *107*, 2411–2502. DOI: 10.1021/cr050989d.

Dondi, M., Matteucci, F., Cruciani, G., Gasparotto, G., & Tobaldi, D. M. (2007). Pseudobrookite ceramic pigments: Crystal structural, optical and technological properties. *Solid State Sciences*, *9*, 362–369. DOI: 10.1016/j.solidstatesciences.2007.03.001.

dos Santos, J. B., da Silva, F. L., Altino, F. M. R. S., da Silva Moreira, T., Meneghetti, M. R., & Meneghetti, S. M. P. (2013). Cellulose conversion in the presence of catalysts based on Sn(IV). *Catalysis Science & Technology*, *3*, 673–678. DOI: 10.1039/c2cy20457f.

Fajardo, H. V., Longo, E., Probst, L. F. D., Valentini, A., Carreño, N. L. V., Nunes, M. R., Maciel, A. P., & Leite, E. R. (2008). Influence of rare earth doping on the structural and catalytic properties of nanostructured tin oxide. *Nanoscale Research Letters*, *3*, 194–199. DOI: 10.1007/s11671-008-9135-3.

Girisuta, B., Janssen, L. P. B. M., & Heeres, H. J. (2007). Kinetic study on the acid-catalyzed hydrolysis of cellulose to levulinic acid. *Industrial & Engineering Chemistry Research*, *46*, 1696–1708. DOI: 10.1021/ie061186z.

Huber, G. W., Iborra, S., & Corma, A. (2006). Synthesis of transportation fuels from biomass: Chemistry, catalysts, and engineering. *Chemical Reviews*, *106*, 4044–4098. DOI: 10.1021/cr068360d.

Kemdeo, S. M., Sapkal, V. S., & Chaudhari, G. N. (2010). TiO_2–SiO_2 mixed oxide supported MoO_3 catalyst: Physicochemical characterization and activities in nitration of phenol. *Journal of Molecular Catalysis A: Chemical*, *323*, 70–77. DOI: 10.1016/j.molcata.2010.03.017.

Komanoya, T., Kobayashi, H., Hara, K., Chun, W. J., & Fukuoka, A. (2011). Catalysis and characterization of carbon-supported ruthenium for cellulose hydrolysis. *Applied Catalysis A: General*, *407*, 188–194. DOI: 10.1016/j.apcata.2011.08.039.

Larson, A. C., & Von Dreele, R. B. (1994). General structure analysis system (GSAS). *Los Alamos National Laboratory Report LAUR 86–748*. Los Alamos, NM, USA: Los Alamos National Laboratory.

Luo, C., Wang, S., & Liu, H. (2007). Cellulose conversion into polyols catalyzed by reversibly formed acids and supported ruthenium clusters in hot water. *Angewandte Chemie International Edition*, *46*, 7636–7639. DOI: 10.1002/anie.200702661.

Milao, T. M., de Mendonça, V. R., Araújo, V. D., Avansi, W., Ribeiro, C., Longo, E., & Bernardi, M. I. B. (2012). Microwave hydrothermal synthesis and photocatalytic performance of ZnO and *M*:ZnO nanostructures (M = V, Fe, Co). *Science of Advanced Materials*, *4*, 54–60. DOI: 10.1166/sam.2012.1252.

Oliveira, J. F. A., Milão, T. M., Araújo, V. D., Moreira, M. L., Longo, E., & Bernardi, M. I. B. (2011). Influence of different solvents on the structural, optical and morphological properties of CdS nanoparticles. *Journal of Alloys and Compounds*, *509*, 6880–6883. DOI: 10.1016/j.jallcom.2011.03.171.

Onda, A., Ochi, T., & Yanagisawa, K. (2008). Selective hydrolysis of cellulose into glucose over solid acid catalysts. *Green Chemistry*, *10*, 1033–1037. DOI: 10.1039/b808471h.

Robles-Nuñez, J., Chiñas-Castillo, F., Sanchez-Rubio, M., Lara-Romero, J., Huirache-Acuña, R., Jimenez-Sandoval, S., & Alonso-Nuñez, G. (2012). Improved hydrothermal synthesis of MoS_2 sheathed carbon nanotubes. *Chemical Papers*, *66*, 1130–1136. DOI: 10.2478/s11696-012-0227-2.

Stroppa, D. G., Montoro, L. A., Beltrán, A., Conti, T. G., da Silva, R. O., Andrés, J., Longo, E., Leite, E. R., & Ramirez, A. J. (2009). Unveiling the chemical and morphological features of Sb–SnO_2 nanocrystals by the combined use of high-resolution transmission electron microscopy and ab initio surface energy calculations. *Journal of the American Chemical Society*, *131*, 14544–14548. DOI: 10.1021/ja905896u.

Zhang, Y., Xue, Y., & Yu, M. (2011). Hydrothermal synthesis of core–shell structured PS@$GdPO_4$:Tb^{3+}/Ce^{3+} spherical particles and their luminescence properties. *Chemical Papers*, *65*, 29–35. DOI: 10.2478/s11696-010-0088-5.

Zou, Y. L., Li, Y., Li, J. G., & Xie, W. J. (2012). Hydrothermal synthesis of momordica-like CuO nanostructures using egg white and their characterisation. *Chemical Papers*, *66*, 278–283. DOI: 10.2478/s11696-012-0139-1.